

# **The Corrosion / Electrochemistry of Beryllium and Beryllium Weldments in Aqueous Chloride Environments**

submitted by:

Mary Ann Hill, Darryl P. Butt, R. Scott Lillard

Materials Corrosion and Environmental Effects Lab  
MST-6, Metallurgy  
Materials Science and Technology Division  
Los Alamos National Laboratory  
Los Alamos, New Mexico 87545

October 1, 1996

submitted to:

Doug Kautz

NMT-5  
Nuclear Materials Technology Division  
Los Alamos National Laboratory  
Los Alamos, New Mexico 87545

contributors:

Doug Kautz, LANL  
Brett Kniss, LANL  
George Carlson, LANL  
David Jarboe, LANL  
Tom Taylor, LANL  
Jim LeMay, LLNL  
Jim Oldani, LLNL  
Gary Devine, LLNL  
Janet Hauber, LLNL  
Bill Moddeman, PANTEX

## Executive Summary

The work described in this report details our progress on the beryllium surveillance project during the 1996 fiscal year. Our goals for FY '96 were two-fold: 1) develop a sensor for monitoring the corrosion of beryllium *in situ* and 2) establish baseline electrochemistry / corrosion data on beryllium in aqueous chloride environments. To address security concerns, the data in this report are not stockpile specific. A classified document addressing applicability is in preparation and will be available in early FY '97.

To date we have successfully designed and tested 2 separate corrosion sensors; one for monitoring the corrosion between galvanic couples as a function of time and, another for monitoring polarization resistance as a function of time. Both of these sensors are passive devices and we anticipate their use in the stockpile. Their design is based on a time-of-wetness monitor (ASTM-G84-84). Each monitor consists of two interwoven metal combs mounted in and separated by epoxy. Each fully assembled monitor is approximately 2.5 cm<sup>2</sup> in diameter and can be made as thin as 0.5 cm. The two combs in the galvanic couple monitor are each machined from different materials: one from Be S200F and the other from Al-Si eutectic. Its purpose is to simulate the galvanic couple that exists between Be and the weld material (see below). The onset of corrosion between this galvanic couple is detected by current flow through a zero resistance ammeter. This meter is capable of detecting nanoamperes of current which has proven to allow the detection of extremely fine condensate on the monitor. The combs in the polarization resistance monitor are both made of Be S200F. Its purpose is to monitor changes in the corrosion rate of Be as a function of time. Corrosion rate is monitored by making an impedance measurement between the combs at high frequency (to measure the amount of condensate on the monitor) and low frequency (to measure the polarization resistance). Laboratory measurements have demonstrated that this monitor is sensitive to both the amount of condensate present and the corrosion rate of the Be electrodes.

Because literature on the corrosion - electrochemistry of Be is fairly limited, to address Be surveillance concerns we established baseline data for this material in aqueous chloride environments. In addition, the effects of solution pH were also examined. It was shown that pitting (localized) corrosion of Be occurred in chloride solutions in the pH range of 4-12.5. Chloride solutions of pH less than or equal to 2, active (general) corrosion of the entire Be surface was observed. Furthermore, the passive current densities (anodic dissolution rate) of Be were shown to be lowest in near neutral solutions somewhat higher in alkaline solutions and highest in acidic solutions. Laboratory experiments with bulk materials have also shown that a galvanic couple exists between bulk Be and the Al-Si eutectic used in Be weldments. In this couple Be acts as the sacrificial anode and Al-Si as the protected cathode. Sections cut from an actual Be weld have demonstrated that this couple results in accelerated damage of the bulk Be as well as the small Be precipitate in the weld material. However, because these Be precipitates are so small, no visible damage to the weld is observed.



Executive Summary	ii
List of Tables	vi
List of Figures	vii
<b>BACKGROUND</b>	<b>1</b>
<i>Review of Passivity</i>	1
<i>Beryllium Corrosion</i>	3
<i>Atmospheric Corrosion Monitors</i>	4
<b>EXPERIMENTAL METHODS</b>	<b>6</b>
<b>RESULTS AND DISCUSSION</b>	<b>8</b>
<i>Beryllium Pitting Corrosion in Chloride Solutions</i>	8
<i>Passivity of Beryllium as a Function of pH</i>	9
<i>Galvanic Interaction between Bulk Beryllium and Weld Material</i>	9
<i>Atmospheric Corrosion Monitors</i>	12
<b>REFERENCES</b>	<b>13</b>
<b>TABLES</b>	<b>16</b>
<b>FIGURES</b>	<b>21</b>

## **List of Tables**

Table 1. Typical S200D and S200F Chemistries

Table 2. List of Solutions Used For Experiments

Table 3. Aqueous Corrosion Data from Potentiodynamic Polarization Curves in Deaerated Chloride Solutions, pH=7.0

Table 4. Aqueous Corrosion Data from Potentiodynamic Polarization Curves in Deaerated solutions of various pHs, No Chloride

Table 5. Aqueous Corrosion Data from Potentiodynamic Polarization Curves in Deaerated Solutions, of various pHs, Containing 0.1 M NaCl

## List of Figures

Figure 1. Potential-pH (Pourbaix) diagram for beryllium-water at 25°C (18).

Figure 2. Beryllium polarization curves as a function of chloride concentration showing an increase in pitting potential with an increase in chloride concentration.

Figure 3. Pitting potential as a function of chloride concentration displaying a logarithmic relationship with a slope of -0.064.

Figure 4a. Bright field micrograph showing corrosion pits on S200F Beryllium after potentiodynamic polarization in 0.01 M NaCl.

Figure 4b. Polarized light micrograph showing corrosion pits on S200F Beryllium after potentiodynamic polarization in 0.01 M NaCl.

Figure 5. Scanning electron micrograph of pitted beryllium showing distinct planes in corrosion pits. These planes appear to be the (0001) basal planes.

Figure 6. Beryllium polarization curves as a function of solution pH. Beryllium forms a passive layer and does not pit in the absence of an aggressive species.

Figure 7. Passive current density as a function of pH showing a minimum in the pH range between 7 and 9.

Figure 8. Potentiodynamic polarization curves as a function of chloride concentration and pH. The beryllium pits at pHs of 7 and 12.5 and actively dissolves at pHs of 1 and 2.

Figure 9. Aluminum-Silicon Phase Diagram showing the eutectic at 12.2 at.% Si. (28).

Figure 10. Open circuit potential of Be and Al-Si as a function of time in 0.1 M NaCl under ambient aeration.

Figure 11. Polarization curves of Al-Si and beryllium in 0.1 M NaCl under ambient aeration. If the cathodic line of the aluminum-silicon were extended, it would eventually intersect the anodic curve of the beryllium at the couple current and couple potential.

Figure 12. Couple potential and couple current as a function of time for an aluminum/silicon-beryllium galvanic couple in 0.1 M NaCl under ambient aeration.

Figure 13a. Bright field optical micrograph of beryllium weldment prior to immersion in chloride solution.

Figure 13b. Polarized light optical micrograph of beryllium weldment prior to immersion in chloride solution.

Figure 14. Bright field optical micrograph of beryllium weldment following two hours of immersion in 0.1 M NaCl solution.

Figure 15. Bright field optical micrograph of beryllium weldment following two days of immersion in 0.1 M NaCl solution.

Figure 16. Bright field optical micrograph of beryllium weldment following two days of immersion in 0.1 M NaCl solution.

Figure 17. Preferential attack of beryllium precipitates in Al-Si weld bead.

Figure 18. Diagram representing concentrations of Be precipitates in the weld matrix which are **a)** below the percolation threshold for weld deterioration and **b)** above the percolation threshold for weld deterioration.

Figure 19. Photograph displaying an atmospheric corrosion monitor made of laser machined mild steel and titanium.

Figure 20. Electrochemical impedance microscopy measurements on a beryllium corrosion monitor as compared with a bulk beryllium sample. The bulk sample was submersed in a boric acid/borate (pH=7) solution while a drop of solution approximately 1.6 cm in diameter was placed on the monitor. Results did not differ significantly between the bulk sample and the monitor.

Figure 21. Couple current measured on a titanium/mild steel corrosion monitor. Couple current increases with a decrease in solution pH.



## Background

### *Review of Passivity*

Passivity occurs when the rate of metal dissolution decreases upon increasing the potential to more positive values. The result is low corrosion rates at potentials more positive than the open circuit potential. The nature of passive films from a materials science perspective has been reviewed by Kruger (1). Most passive films are hydrated oxide and are less than 30 angstroms thick (2). For example,  $\text{Fe}_3\text{O}_4$  is a thin passive film which forms on iron when exposed to a borate buffer solution. Ex-situ characterization of passive films (XPS, Auger, TEM, . . .) is difficult as there is always a question of change when a metal is removed from an corrosive environment. Thus, the basic nature of passivity is not well understood. It has been shown that the most protective passive films are vitreous, that is they have no crystallographic lattice, but good short-range order. These factors can be enhanced by alloying and hydration, which improves structural flexibility of the thin film. The electronic properties of passive films vary. Many passive layers are insulating, although some can behave as semiconductors (3-5).

Various theories have been postulated to describe the breakdown of passivity and onset of pitting corrosion in chloride environments. All of these models describe particular aspects of the corrosion process, but no model is universally accepted as a comprehensive theory. Four empirical observations are associated with pitting corrosion: 1) the presence of an aggressive species to initiate pitting, 2) a critical potential or breakdown potential ( $E_{\text{pit}}$ ), 3) an induction time associated with the onset of pitting, and 4) localized sites. Uhlig (6) proposed an explanation for the breakdown of passivity based on adsorption theory. An adsorbed film of oxygen, the passive film, is penetrated by an aggressive species, such as chloride. Once oxygen is displaced, the adsorbed chloride is absorbed into the oxide, which results in the initiation of breakdown due to weakened metal ion-metal bonds in the surface film. Natishan et. al. (7) found that the pH of zero charge,  $\text{pH}_{\text{pzc}}$ , (pH at which the surface oxide has no net charge) can affect the pitting characteristics of the surface oxide.

At pHs lower than  $\text{pH}_{\text{pzc}}$ , the surface behaves as Lewis acids. Lewis bases, such as chloride, are attracted to this surface and can adsorb. At pHs greater than  $\text{pH}_{\text{pzc}}$ , the surface behaves as a Lewis base and as a result Lewis bases are repelled. Once absorbed, chloride migrates to the metal/oxide interface and breakdown ensues. Wood et. al. (8) describes the breakdown of the passive film as resulting from flaws in the film. These flaws may be due to impurities and segregated phases or mechanical flaws, such as those that may be formed during the stress-relief process in the oxide. Below  $E_{\text{pit}}$ , any crack/defect which is formed in the oxide repassivates. Above  $E_{\text{pit}}$ , a crack/defect which forms in the oxide becomes a corrosion pit. This process is often referred to as the crack-heal mechanism. Wood claims that the rate at which chloride penetrates surface films at flaws overrides the effect of chloride interaction with the passive film (described in displacement and migration models). The ion migration model, developed by Pryor (9), describes the process by which ions migrate through anion and cation vacancies in an oxide. For aluminum, electrical neutrality is reached when one aluminum ion ( $\text{Al}^{+++}$ ) from the lattice passes into solution for every three chloride ions (replacing three oxygen ions) in the surface film. This reaction creates uncharged cation vacancies which permit aluminum ions to move through the oxide film. Migration is accelerated by an applied field across the oxide. Breakdown of passivity occurs when chloride reaches the metal/oxide interface.

Investigators have also described other mechanisms for pitting including: film thinning, precursive blistering, and metastable pitting. The film dissolution model of Foley (10) is based upon experiments in which an alpha aluminum oxide physically dissolves in chloride solution. Barger and Givens (11,12) found that blister formation in anodized aluminum can occur in aqueous chloride solutions as a precursor to pit formation. They proposed that above  $E_{\text{pit}}$ , chloride penetrates the oxide to the metal interface where both the anodic and cathodic reactions take place. A blister forms/develops under the oxide due to the forces associated with trapped  $\text{H}_2$  from the local cathodic reaction. The time it takes from formation of the blister to rupture is dependent upon oxide thickness, chloride ion

concentration, and the specimen potential relative to the pitting potential of the sample. Metastable pitting has been described by several researchers (13-17). This mechanism, based on Wood's crack/heal mechanism, describes the formation of pits and repassivation of pits below the pitting potential. The frequency of the pits increases when approaching the pitting potential and the probability of stable pitting is directly related to the frequency and intensity of metastable pitting. Breakdown occurs when a critical combination of pit radius/depth and current density is reached at the pitting potential.

### *Beryllium Corrosion*

Beryllium has a hexagonal close packed structure (hcp), high specific heat and thermal conductivity, and high specific strength and stiffness. It is an attractive engineering material for nuclear applications due to its low neutron cross section and for aerospace applications because of its low density. Disadvantages to using beryllium include toxicity in particulate form, low fracture toughness, and high cost. The passivity of beryllium has been shown to be controlled by a thin surface film of BeO or its hydrate ( $\text{BeO} \cdot (\text{H}_2\text{O})_x$ ). The potential-pH or Pourbaix diagram for beryllium-water is shown in Figure 1 (18). In the presence of highly acidic solutions, hydrogen is evolved as the water decomposes and beryllium anodically reacts to form  $\text{Be}^{++}$ . In strongly alkaline solutions, hydrogen evolves and soluble  $\text{Be}_2\text{O}_3^{--}$  and  $\text{BeO}_2^{--}$  anions form. At neutral pHs, a protective layer of  $\text{Be}(\text{OH})_2$  forms on the surface of the beryllium. Gulbrandsen et. al. (19), who has studied the passive behavior of beryllium in solutions pH 1-15, demonstrated that the passive current density was minimum in solution pH 11 and increased logarithmically in more acidic and alkaline solutions. Further, there was some evidence that oxygen evolution on BeO occurred suggesting BeO is a semiconductor. Mueller (20) discussed two primary causes of beryllium corrosion in humid atmospheres. First, beryllium carbide impurities in beryllium will react with water in the atmosphere to form beryllium oxide. Second, surface contamination from chloride and sulfate will lead to localized corrosion. Levy (21) noted pitting in beryllium at the open circuit potential when exposed to 0.1 M NaCl solution.

However, it is interesting to note that stress corrosion cracking (SCC) of beryllium has not been observed. For example, studies of beryllium in 5% sodium chloride solution using c-bend samples stressed to 80% of the yield strength indicated that beryllium was not susceptible to SCC (22).

Beryllium is difficult to weld because it is highly susceptible to cracking. Cracking in beryllium may arise from defects, such as inclusions and porosity, hot cracking, which is attributed to an aluminum-rich grain boundary film resulting from rejection of the aluminum during solidification, and thermal stresses due to the ductility anisotropy in beryllium. Beryllium has been successfully welded using Al-Si filler metal with more than 30 wt.% Al (23). This filler creates an aluminum-rich fusion zone with a low melting point that tends to backfill cracks. Drawbacks to adding a filler metal include a reduction in service temperature, a lowering of the tensile strength of the weld, and the possibility for galvanic corrosion to occur at the weld. The galvanic corrosion of beryllium weldments exposed to humid environments can be monitored in the actual environment of the weld by atmospheric corrosion monitors.

#### *Atmospheric Corrosion Monitors*

Atmospheric Corrosion is defined by the very thin electrolyte that forms on the surface of the material. This electrolyte may contain salts from the environment in a concentrated form. It differs from aqueous corrosion in that the thin layer of electrolyte readily allows oxygen (the cathodic reaction species) from the atmosphere to diffuse to the surface of the material at higher rates than occur in bulk solutions. Higher oxygen concentrations at the surface allow the corrosion rate in the atmospheric case to occur at a higher rate than would ordinarily occur in an aqueous solution as these rates are often cathodically limited. Therefore, the practice of estimating atmospheric corrosion rates by using an aqueous environment to simulate atmospheric corrosion is non-conservative; i.e. it can greatly underestimate the actual corrosion rates. The term atmosphere is used here to define the exposure conditions which exist inside storage vessels.

The main advantages of the Atmospheric Corrosion Monitors (ACM) are: 1) compact size, 2) allow continuous monitoring of corrosion rates, and 3) may be placed in the actual environment of a component or attached directly to a component. The capability of an ACM to measure corrosion rates in the true environmental conditions is an obvious advantage compared to other methods such as aqueous corrosion or accelerated chamber techniques because the data obtained from an ACM does not require extrapolation; thus the ACM yields the actual corrosion rate for the material in the environment of concern. The three ACM's we proposed to use for the Be Surveillance project are discussed below in detail. It should be noted that while ACM's are designed for exposure to the same environment as the engineering material, there is nothing that precludes their use in an accelerated corrosion chamber.

The Atmospheric Electrochemical Impedance Spectroscopy monitor (ATMEIS) was designed primarily to be used to assess the degradation of coated metals. It consists of a sample which is coated in the same manner as the engineering sample. Once the coating is fully cured, a thin (less than 1  $\mu\text{m}$ ) gold grid is sputter deposited onto the surface of the coating making a gold-coating-metal sandwich. Electrical contact is made to the metal substrate and to the gold grid. This gold grid acts as a counter electrode enabling a two-electrode Electrochemical Impedance Spectroscopy (EIS) measurement to be made across the coating.

The Atmospheric Corrosion Rate Monitor (ACRM) was designed primarily to measure the corrosion rates of bare metal surface under atmospheric conditions. It consists of two interwoven "combs" of candidate metal (e.g., Be) separated by an insulator such as epoxy or mylar. Electrical contact is made to each of the two pieces of metal. If humidity is present in the atmosphere, a thin layer of electrolyte will precipitate onto the surface creating a liquid junction between the metal combs. The polarization resistance of the probe materials in the environment to which it is exposed is then measured as a function of time using either an EIS or dc technique.

The Galvanic Couple Monitor (GCM) is used to measure the corrosion rate between two dissimilar metals which act as a galvanic couple. The GCM consists of the two interwoven combs of candidate metals (i.e. Be / weld-material) separated by an insulator (as above). This couple may or may not be covered with a coating depending on the desired data. Electrical contact is made to each of the two pieces of metal through a Zero Resistance Ammeter (ZRA). If a water layer forms on the exposed surface, a galvanic couple is established and the current between the two is inventoried with the ZRA. This measured current is the corrosion current and can be related to corrosion rate using Faraday's law.

### **Experimental Methods**

Electrodes were made from S200F beryllium discs with a surface area of 1.43 cm<sup>2</sup>. A typical analysis of S200F vs. S200D beryllium is shown in Table 1. Aluminum-silicon electrodes were made from as-cast material. The purity of the aluminum was 99.999% and the silicon lump was 98.5% pure with the remainder consisting primarily of iron. These purity levels are typical of those found in beryllium welds. The surface area of the Al-Si electrodes was 1.6-1.8 cm<sup>2</sup>. Electrical leads were connected to the back of the samples with silver paint and epoxy. The electrical leads were encapsulated in a glass tube and the samples were mounted in 2.5 cm diameter Struers® epoxy mounts. All beryllium samples were ground to 400 grit SiC paper. Aluminum-silicon was prepared on one micron diamond.

The test solutions that were used in corrosion experiments are listed in Table 2. All solutions were mixed with twice distilled deionized water and kept at room temperature (25°C). Chloride containing solutions were mixed with AnalR Grade sodium salts. The pH values reported were measured with a calibrated Corning 320® pH meter. Deaeration was accomplished with ultra high purity argon for a minimum of six hours prior to running experiments.

The electrolyte volume for all experiments was 500 ml. A platinum counter electrode and a reference electrode were placed in the cell. The reference electrode was either a mercury/mercurous sulfate (MMSE) electrode for chloride-free solutions or a saturated calomel electrode (SCE) for solutions containing chloride. Electrochemical measurements were made using an EG&G PAR Potentiostat/Galvanostat Model 263A or an EG&G Versastat®, computer controlled by Corrware®. Samples were left at open circuit for one hour prior to running potentiodynamic polarization curves to ensure steady state. The scan rate for the polarization curves was 0.1 mV/sec. All curves were run from 100 mV below the open circuit potential to 1 V above the open circuit potential and reversed back to open circuit at a current of  $1 \times 10^{-3}$  amps. Data were acquired at 1 mV/point. A 5.3 Hz low pass filter was used to minimize noise.

ACRMs were constructed from beryllium combs and GCMs were made from both beryllium and aluminum-silicon combs. The beryllium used to fabricate the ACMs was electrically discharge machined (EDM) while the aluminum-silicon was laser machined. To ensure that the beryllium and aluminum-silicon were not in contact with one another, 0.1 mm mylar shims were placed between each tine. The probe fingers were 7.8 mm long, 0.6 mm wide, and 0.2 mm apart. The entire probe was 1.6 cm long and 1.2 cm wide. Leads were attached using silver paint and epoxy. Holes were drilled in the sides of mold cups to allow the ends of the leads to protrude from the sides of the mounts. Monitors were then mounted in 32 mm diameter epoxy. The monitors were ground and polished to 0.3 micron diamond. EIS measurements on the monitors were conducted in a two electrode configuration, i.e. one lead was connected to the working electrode and the other two leads were connected to both the counter and reference electrodes.

## Results and Discussion

### *Beryllium Pitting Corrosion in Chloride Solutions*

Figure 2 shows potentiodynamic polarization curves for S200F beryllium electrodes in deaerated salt solutions ranging in concentration from  $10^{-4}$  to  $10^{-1}$  M NaCl. Beryllium is passive in these solutions until reaching a pitting potential. The pitting potential is noted by a sharp rise in the current density. The values for the open circuit potential, pitting potential, and passive current density for each curve are listed in Table 3. The pitting potential, or breakdown potential, increased logarithmically with an increasing chloride concentration as shown in Figure 3. The slope of the line is -0.064, so the change in the pitting potential from  $10^{-4}$  to  $10^{-1}$  M NaCl is approximately 64 mV. A similar relationship has been noted in aluminum (11, 17, 24, 25). For comparison, a sample of S200D beryllium was also tested in a solution of 0.1 M NaCl. The pitting potential of this sample was -0.931 V vs. SCE, essentially the same as that found for S200F beryllium.

One outcome of the pitting experiments was the finding that beryllium appears to corrode preferentially at certain orientations. Figures 4a and 4b show optical beryllium micrographs in bright field and polarized light, respectively. From these micrographs, it is difficult to determine if pitting has preferentially initiated at grains with specific orientations as the pits are large and encompass many grains. Figure 5 shows a scanning electron micrograph of corrosion pits in S200F beryllium following a polarization experiment in 0.01 M NaCl solution. Specific planes have corroded away while others remain intact. It is presumed that the (0001) basal planes do not corrode as readily as other orientations since these are the most closely packed planes in the lattice. Thus, corrosion appears to occur more rapidly between and parallel to the (0001) planes. Increased resistance to pitting corrosion on the most closely packed crystallographic planes has been discovered in studies with zinc (26) and beta-tin (27) monocrystals. We are currently investigating this apparent effect of beryllium orientation on pitting using Orientation Imaging Microscopy (OIM) combined with careful identification of pitting sites.

### *Passivity of Beryllium as a Function of pH*

Beryllium polarization curves as a function of pH are shown in Figure 6 and data are listed in Table 4. Low anodic dissolution rates (less than  $1 \times 10^{-6}$  A/cm<sup>2</sup>) are associated with the oxide which forms on beryllium in this pH range. The relationship between passive current density and solution pH is plotted in Figure 7. A minimum in the curve exists in the pH range between 7-9. This differs from Gulbrandsen's result where the minimum in the passive current density was in the vicinity of pH 11. Gulbrandsen also noted an increase in the current density above the oxygen evolution potential and concluded that the BeO protective layer may behave as a semiconductor. However, the experiments in this report were not taken to a high enough potential to observe this phenomena so it is difficult to comment on the electronic nature of the passive layer without further experiments.

Figure 8 presents the polarization curves for beryllium in deaerated 0.1 M NaCl as a function of solution pH. Beryllium actively corrodes at the open circuit potential in 0.1 M NaCl solutions with a pH of 2.0 or less. The surface of the samples exposed at pH values of 1-2 in chloride solution did not appear pitted, instead the sample surfaces were black. The black deposit is most likely BeO. This surface will be characterized by X-ray photoelectron spectroscopy (XPS) to confirm the composition of this black surface layer.

### *Galvanic Interaction between Bulk Beryllium and Weld Material*

The most commonly used filler metal in beryllium welds is Al-12 wt.% Si. This is in close proximity to the eutectic composition which provides a low melting point and adequate fluidity. The Al-Si phase diagram is shown in Figure 9 (28). The open circuit potentials, at ambient aeration in 0.1 M NaCl solution, of beryllium and aluminum-silicon are shown in Figure 10. As seen in this figure, the beryllium open circuit potential is more negative than that of aluminum-silicon. Thus, when coupled under these conditions, beryllium will act as the anode and aluminum-silicon acts as the cathode. Polarization

curves for these two metals, at ambient aeration in 0.1 M NaCl solution, are shown in Figure 11.

To measure the couple current, the beryllium was connected to the black or negative lead of a zero resistance ammeter (ZRA) while the aluminum-silicon was connected to the red or positive lead. Electron flow was from the beryllium anode to the aluminum-silicon cathode. For the couple potential, an SCE electrode was connected to the ground lead of a digital multimeter, while the aluminum-silicon was connected to the positive lead. The couple current and couple potential which resulted is shown in Figure 12. To simulate the galvanic interactions that may occur in a weld, separate electrodes were fabricated from beryllium and aluminum/silicon. These electrodes were placed in a single cell containing 0.01 M NaCl. This data implies that beryllium will corrode preferentially when galvanically coupled with aluminum-silicon and acts as a sacrificial anode; i.e. beryllium is consumed while the aluminum-silicon is protected.

To evaluate the degree of interaction between Be and Al-Si in an actual weld, sections from a beryllium weldment were exposed to 0.1M Cl<sup>-</sup> solution. Prior to immersion in Cl<sup>-</sup>, both bright field and polarized light micrographs of the Be weldment were taken (Figures 13a and 13b, respectively). As shown in these micrographs, the Al-Si weld material contains a high percentage of very small (less than 2  $\mu\text{m}$  in diameter) pure Be precipitate as well as porosity from the weld process. The columnar grains surrounding the weld (Figure 13b) define the heat affected zone in the material. Not surprisingly, this zone appears to be larger near the surface of the joint than at the base.

A bright field micrograph of this weldment after 2 hours of immersion in 0.1M NaCl is shown in Figure 14. Little attack of the Be or weld material was observed. A similar micrograph of this weldment after approximately 48 hours of immersion is shown in Figure 15. Large scale pitting attack of the Be parent material was observed. No attack of the weld material was apparent at this magnification. Surprisingly, no attack of the heated affected zone was apparent. This phenomena can be seen more clearly at higher

magnification in Figure 16. While the absence of attack in this region is not wholly understood, it is not believed to owe to the formation of a corrosion resistant alloy between the Be and weld material as the solid solubility of Be in Al and/or Si is almost nonexistent. Further XPS, EDAX and AUGER analysis of this region is ongoing. Even higher magnification (Figure 17) reveals that some preferential attack of the Be precipitates in the Al-Si weld material, not apparent at lower magnifications, has occurred. This attack appears to be limited to fine Be dendrites in the weld material. Once an individual Be precipitate has been fully removed the corrosion process appears to halt, as no additional corrosion of the weld matrix is observed. In addition, the attack of these precipitates appears to be somewhat less than that observed in the bulk Be material.

Collectively, these results indicate that the galvanic couple between Be and the Al-Si weld material results in the cathodic protection of the weld and of the anodic dissolution of the bulk Be material. While the cathodic protection of Al is generally inefficient (as the oxide on Al is an insulator), the high anodic dissolution rate of the bulk Be during pitting corrosion combined with the insulating properties of the Be oxide afford some protection of the Al-Si weld material. Although dissolution of the Be precipitate in the weld material does occur, no corrosion of the Al-Si matrix was observed. The integrity of the weld is, therefore, controlled by what is commonly referred to as a percolation threshold (29-30); i.e. the concentration of Be precipitate in the weld material. Because the only species in the weld susceptible to attack is the Be precipitate, below some threshold in concentration the Be is completely surrounded by Al-Si (except at the surface). Once the Be precipitate has dissolved out, no further corrosion of the Al-Si takes place (Figure 18a). Thus the bulk integrity of the weld is maintained. Above this threshold concentration, percolation of corrosion through the entire weld is sustained by adjacent Be precipitates which are, in part, surrounded by other Be precipitates and are no longer entirely surrounded by Al-Si (Figure 18b).

### *Atmospheric Corrosion Monitors*

Studies involving atmospheric corrosion monitors are preliminary and are aimed at understanding the accuracy of corrosion monitors for determining corrosion rates. Beryllium/beryllium monitors were constructed to measure the beryllium polarization resistance in humid environments. An example of this corrosion monitor is shown in Figure 19. To test the accuracy of the monitors, electrochemical impedance spectroscopy measurements were made on this monitor under two differing conditions: 1) exposed to a 1.6 cm<sup>2</sup> drop of boric acid/borate solution, and 2) submersed in boric acid/borate solution. These results are shown in Figure 20 in the form of Bode magnitude plots. The flat portion of the curve at low frequencies is equal to the sum of the ohmic and interfacial resistance. The flat portion of the curve at high frequencies is equal to the ohmic resistance, also called the solution resistance. As shown in this figure, good correlation between the sample exposed to a drop of solution and the immersed sample was obtained.

Because the reference and counter electrodes were hooked up to the same lead of the corrosion monitor, to obtain the actual result for the sum of the ohmic and interfacial resistance the value read from the plot must be divided by two. This value is equal to  $1.75 \times 10^5$  ohms-cm<sup>2</sup> using the ACM, as compared to  $1.5 \times 10^5$  ohms-cm<sup>2</sup> for bulk beryllium. These numbers can be used to calculate the corrosion current density,  $i_{\text{corr}}$ , using the Tafel equation:

$$i_{\text{corr}} = \beta_a \beta_c / [2.3(\beta_a + \beta_c) R_p],$$

where  $\beta_a$  and  $\beta_c$  are the Tafel slopes of the anodic and cathodic reactions, respectively.  $R_p$  is the Polarization Resistance in ohms-cm<sup>2</sup> and  $i_{\text{corr}}$  is in amps/cm<sup>2</sup>. This expression can be simplified to

$$i_{\text{corr}} = B/R_p,$$

where B is the polarization resistance constant. Once  $i_{\text{corr}}$  is known, corrosion rates can be calculated using the following expression based on Faraday's law:

$$\text{Penetration Rate} = 0.129 a i_{\text{corr}}/nD \quad \text{mpy (mils per year)}$$

where  $a$  is the atomic weight,  $i_{\text{corr}}$  is the current density in  $\mu\text{amps}/\text{cm}^2$ ,  $n$  is the valence charge, and  $D$  is the density in  $\text{gms}/\text{cm}^3$ . This relationship assumes the anodic and cathodic slopes to be 0.12, which is a good estimate. From this equation, the corrosion rate is 0.0467 mpy using the ACM and 0.05445 mpy for the bulk beryllium, a 14% difference between the two measurements.

A prototype corrosion galvanic couple monitor was constructed from titanium/mild steel (Figure 19) and the couple current was measured between the two metals. As shown in figure 21, when placed in a humid environment, a condensate on the monitor results in a measurable current through the ZRA. Similarly, once the condensate evaporates, the couple current falls to zero. Galvanic couple monitors are currently being constructed from beryllium and aluminum/silicon.

## References

1. J. Kruger, *International Materials Reviews*, **33**, 113 (1988).
2. M. G. Fontana and N. D. Greene, *Corrosion Engineering*, 2nd ed., McGraw-Hill Book Company, New York, 321 (1978).
3. F. M. Delnick and N. Hackerman: in *Passivity of Metals* (ed. R. P. Frankenthal and J. Kruger), Princeton, NJ, The Electrochemical Society, 116-133 (1978).
4. E. K. Oshe, J. L. Rosenfeld, and V. C. Doroskenko, *Dokl. Akad. Nauk SSSR*, **194**, 612-614 (1970).
5. W. Schmickler: in *Passivity of Metals* (ed. R. P. Frankenthal and J. Kruger), 102-115: (1978), Princeton, NJ, The Electrochemical Society.
6. H. Uhlig, *Chem. Eng. News*, **24**, 3154 (1946).
7. P. M. Natishan, E. McCafferty, and G. K. Hubler, *J. Electrochem. Soc.*, **135**, 321, (1988).

8. G. C. Wood, W. H. Sutton, J. A. Richardson, T. N. K. Riley, and A. G. Malherbe, in *Localized Corrosion*, R. W. Staehle, B. F. Brown, J. Kruger, and A. Argawal, eds., NACE, Houston, 526, (1971).
9. M. J. Pryor, in *Localized Corrosion*, R. W. Staehle, B. F. Brown, J. Kruger, and A. Argawal, eds., NACE, Houston, 2, (1971).
10. R. T. Foley, *Corrosion*, **42**, 277 (1986).
11. C. B. Barger and R. B. Givens, *Corrosion*, **36**, 618, (1980).
12. C. B. Barger and R. B. Givens, *Journal of the Electrochemical Society*, **124**, 1845, (1977).
13. R. Hollinger and H. Bohni, in *Proceedings of the Symposium on Computer Aided Acquisition and Analysis of Corrosion Data*, M. W. Kendig, U. Bertocci, and J. E. Strutt, Editors, PV 85-3, The Electrochemical Society Proceedings Series, Pennington, NJ, 200 (1985).
14. D. E. Williams, J. Stewart, and P. H. Balkwill, in *Critical Factors in Localized Corrosion*, G. S. Frankel and R. C. Newman, Editors PV 92-9, The Electrochemical Society Proceedings Series, Pennington, NJ, 36 (1992).
15. G. S. Frankel, L. Stockert, F. Hunkeler, and H. Bohni, *Corrosion*, **43**, 429 (1987).
16. P. C. Pistorius and G. T. Burstein, *Phil. Trans. R. Soc. Land, A*, **341**, 531 (1992).
17. S. T. Pride, J. R. Scully, and J. L. Hudson, *J. Electrochem. Soc.*, **141**, 3028 (1994).
18. M. Pourbaix, "Atlas of Electrochemical Equilibria in Aqueous Solutions," Pergamon Press, New York, 135 (1966).
19. E. Gulbrandsen and A. M. J. Johansen, *Corrosion Science*, **36**, 1523 (1994).
20. J. J. Mueller and D. R. Adolphson, in *Beryllium Science and Technology*, **2** (ed. D. R. Floyd and J. N. Lowe), Plenum Press, New York, 417 (1979).
21. D. J. Levy, The Electrolytic Polarization of Beryllium, Lockheed Missiles and Space Technical Report No. 6-90-61-75, (1961).

22. D. D. Hornbacher, The Susceptibility of Beryllium to Stress Corrosion Cracking, CPRD 9:0336-117, The Dow Chemical Company, (1968).
23. G. K. Hicken and W. B. Sample, Jr., *Welding Journal* , **46**, 541s-550s (1967).
24. J. R. Galvele and S. M. De Micheli, *Corrosion Science*, **10**, 795 (1970).
25. Z. A. Foroulis and M. J. Thubrikar, *Electrochimica Acta*, **21**, 225 (1976).
26. R. Guo, F. Weinberg, and D. Tromans, *Corrosion Science*, **51**, 56 (1995).
27. R. Guo, F. Weinberg, and D. Tromans, *Corrosion Science*, **51**, 212 (1995).
28. J. L. Murray and A. J. McAlister, in *Binary Alloy Phase Diagrams*, 2nd ed., ed. T. B. Massalski, ASM International, Metals Park, Ohio, 212, (1990).
29. K. Sieradzki, R.R. Corderman, K Shukla, *Philosophical Magazine A*, vol. 59, no 4, pp 713-46, 1989.
30. S. Qian, R.C. Newman, R.A. Cottis, K Sieradzki, *Journal of the Electrochemical Society*, vol. 137, no. 2, pp 435-39, 1990.

## Tables

Table 1. Typical S200D and S200F Chemistries.

Constituents	S200F	S200D
Beryllium	98.5	98.0
Beryllium Oxide (BeO)	1.5	2.0
Aluminum	0.10	0.16
Carbon	0.15	0.15
Iron	0.13	0.18
Magnesium	0.08	0.08
Silicon	0.06	0.08
Other Metallic Impurities	0.04	0.04

All values are given in weight percent.

Table 2. List of Solutions Used for Experiments.

Chloride Solutions
$10^{-1}$ M NaCl
$10^{-2}$ M NaCl
$10^{-3}$ M NaCl
$10^{-4}$ M NaCl
Various pH Solutions (No Chloride)
0.1 M Tartaric Acid (pH=2)
0.25 M Boric Acid (pH=4.6)
0.05 M Sodium Borate-0.5 M Boric Acid (pH=7)
0.025 M Sodium Borate-0.05 M NaOH (pH=10.7)
NaOH (pH=12.5)
Various pH Solutions (With Chloride)
0.1 M HCl (pH=1)
0.1 M Tartaric Acid + 0.1 M NaCl (pH=2)
0.1 M NaCl (pH=7)
NaOH + 0.1 M NaCl (pH=12.5)

Table 3. Aqueous Corrosion Data from Potentiodynamic Polarization Curves in Deaerated Chloride Solutions, pH=7.0.

Solution	Open Circuit Potential (V vs. SCE)	Pitting Potential (V vs. SCE)	Passive Current Density (amps/cm <sup>2</sup> )
0.1 M NaCl	-1.08198 ± 0.0719	-0.94833 ± 0.00620	1.6693e-07 ± 1.31e-07
0.01 M NaCl	-0.948326 ± 0.0606	-0.88327 ± 0.0250	2.8027e-07 ± 2.77e-07
0.001 M NaCl	-1.04479 ± 0.0326	-0.80310 ± 0.0326	2.6937e-07 ± 1.07e-07
0.0001 M NaCl	-1.15354 ± 0.00998	-0.77278 ± 0.0421	7.0707e-07 ± 1.99e-07

Three tests were run in each of the solutions above, with the exception of 0.0001 M NaCl. Only two tests were run in this solution.

Table 4. Aqueous Corrosion Data from Potentiodynamic Polarization Curves in Various pH Solutions, No Chloride.

Solution pH	Open Circuit Potential (V vs. MMSE)	Passive Current Density (amps/cm <sup>2</sup> )
2.0	$-1.09386 \pm 0.00621$	$7.9020\text{e-}07 \pm 0.00968\text{e-}07$
4.6	$-1.18316 \pm 0.199$	$4.4284\text{e-}07 \pm 0.103\text{e-}07$
7.0	$-1.23308 \pm 0.419$	$3.9028\text{e-}07 \pm 0.209\text{e-}07$
10.7	$-1.68236 \pm 0.0197$	$4.3601\text{e-}07 \pm 0.311\text{e-}07$
12.5	$-1.41828 \pm 0.188$	$7.7817\text{e-}07 \pm 1.52\text{e-}07$

Two tests were run in each solution with the exception of the 12.5 solution. Three tests were run in this solution.

Table 5. Aqueous Corrosion Data from Potentiodynamic Polarization Curves in Deaerated Chloride Solutions at various pHs.

Solution pH	Open Circuit Potential (V vs. SCE)	Pitting Potential (V vs. SCE)	Passive Current Density (amps/cm <sup>2</sup> )
1.0	-0.955725	-0.955725	-----
2.0	-0.959155	-0.959155	-----
7.0	-1.15368	-0.951550	3.1622e-07
12.5	-1.34716	-0.925328	7.9831e-07

The solutions above all contain 0.1 M NaCl. Only one experiment was run in each solution.

# Figures

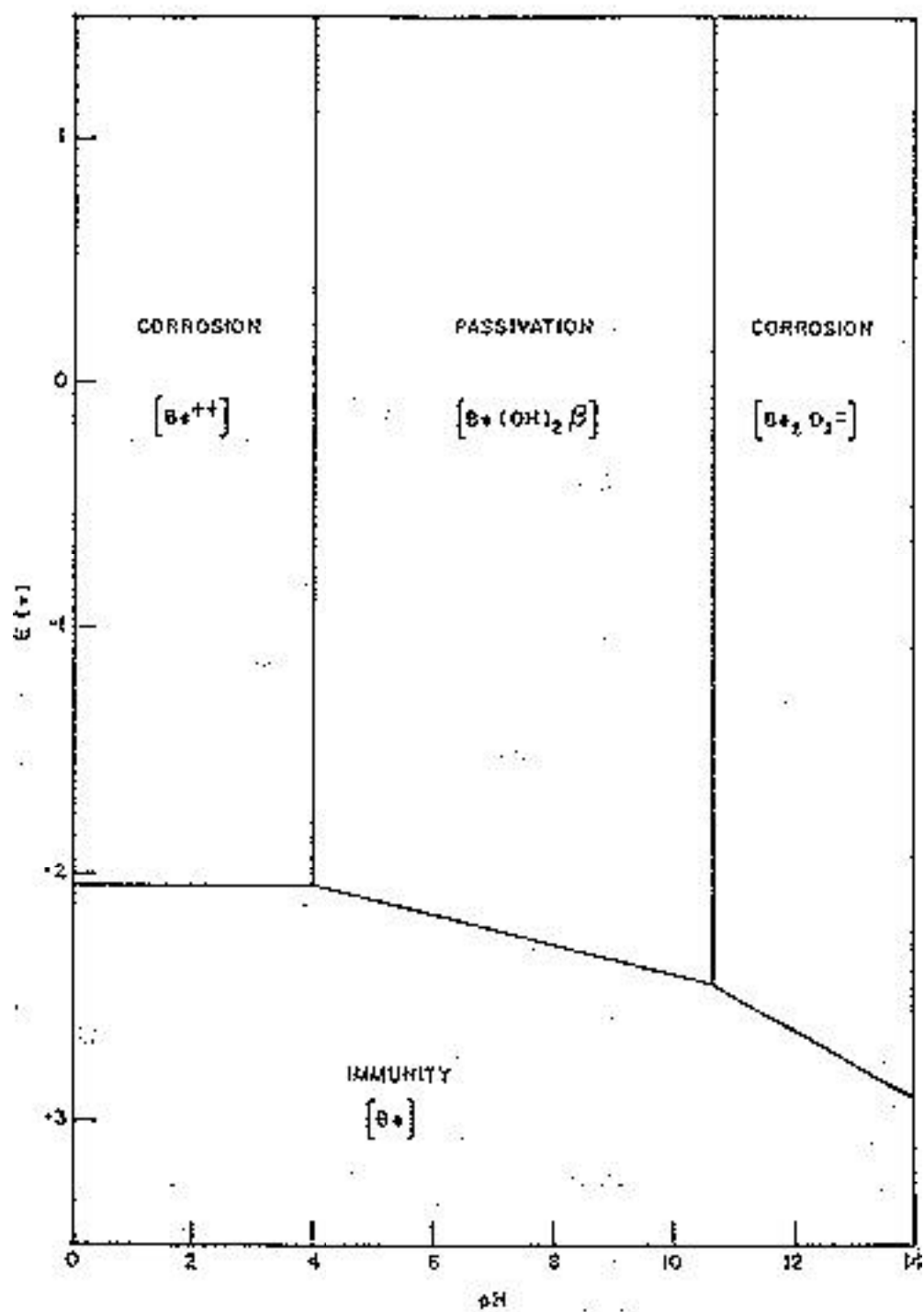


Figure 1. Potential-pH (Pourbaix) diagram for beryllium-water at 25°C (18).

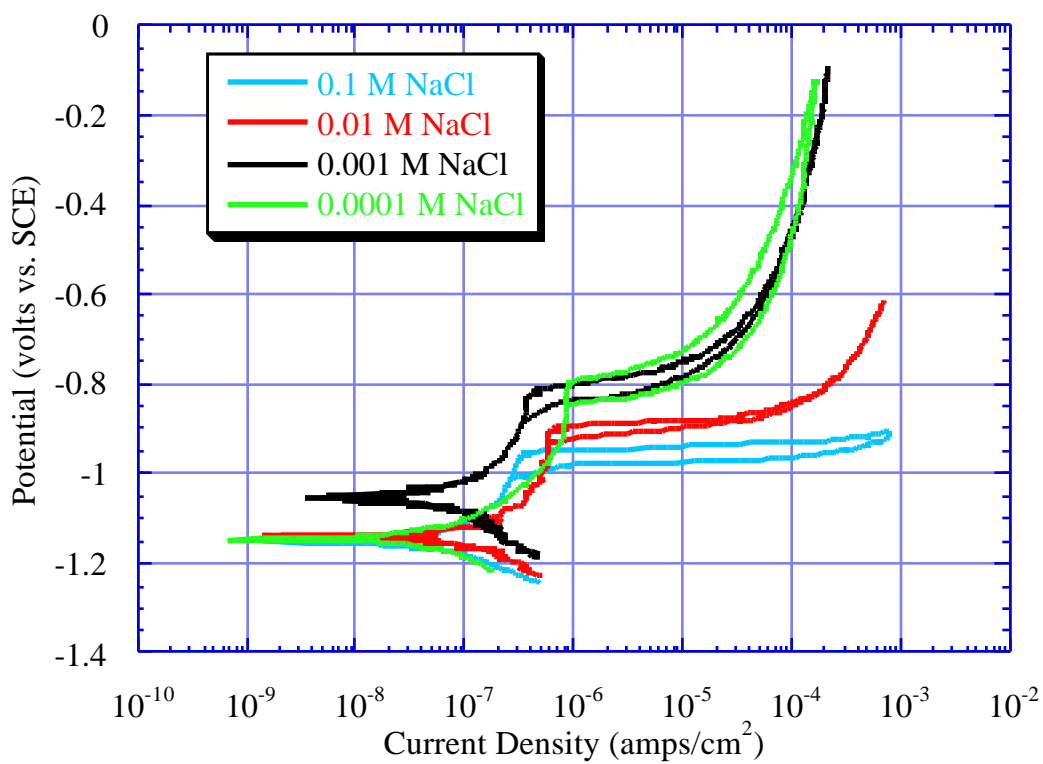


Figure 2. Beryllium polarization curves as a function of chloride concentration showing an increase in pitting potential with an increase in chloride concentration.

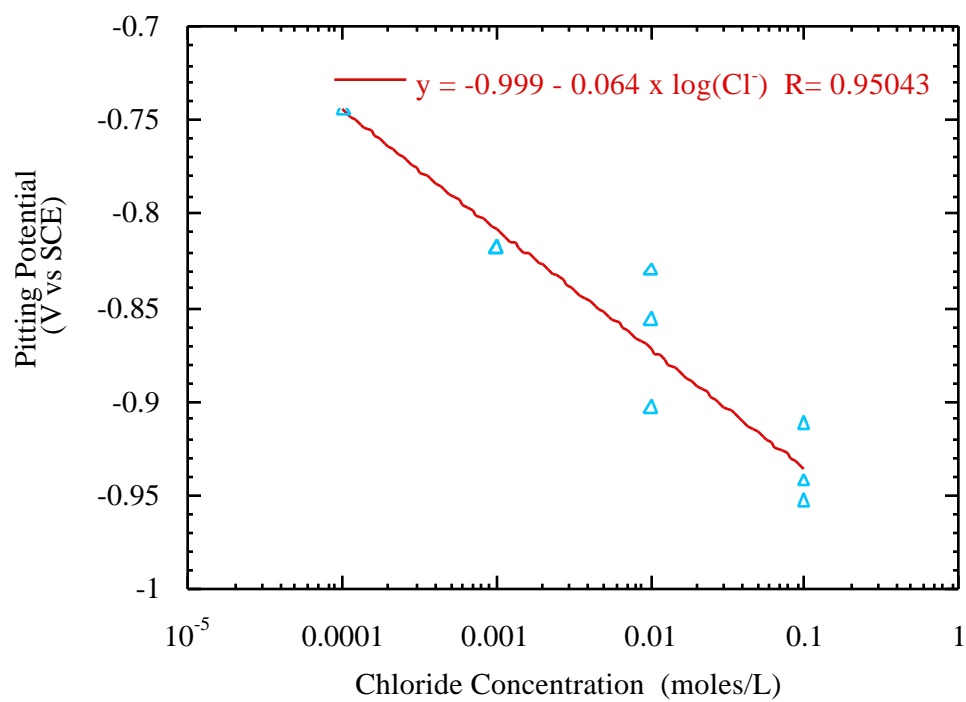


Figure 3. Pitting potential as a function of chloride concentration displaying a logarithmic relationship with a slope of -0.064.

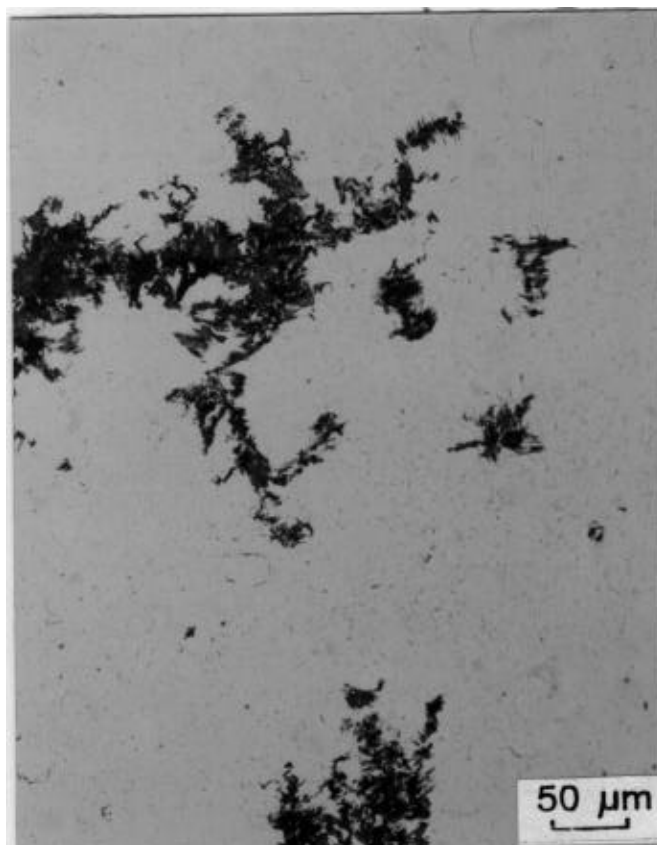


Figure 4a. Bright field optical micrograph showing corrosion pits on S200F Beryllium after potentiodynamic polarization in 0.01 M NaCl.

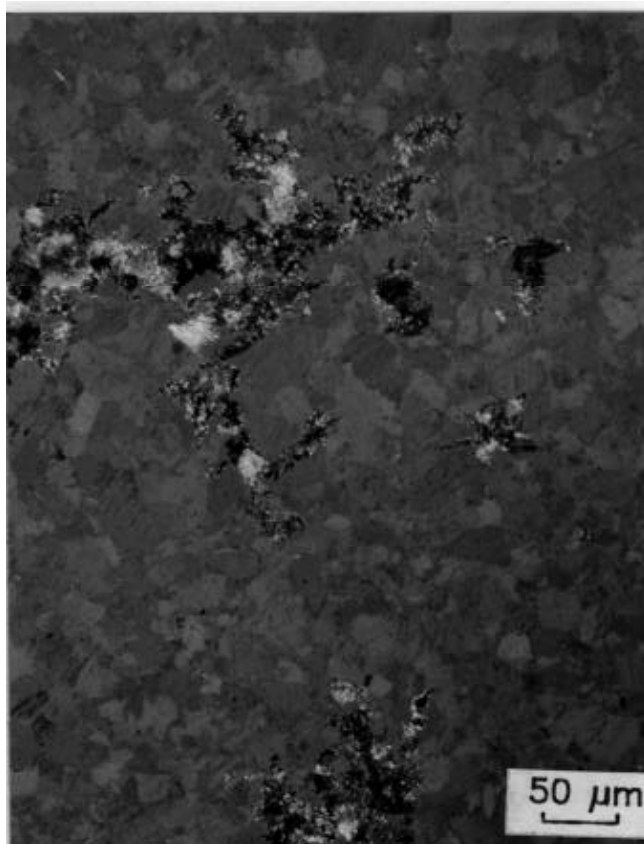


Figure 4b. Polarized light optical micrograph showing corrosion pits on S200F Beryllium after potentiodynamic polarization in 0.01 M NaCl.

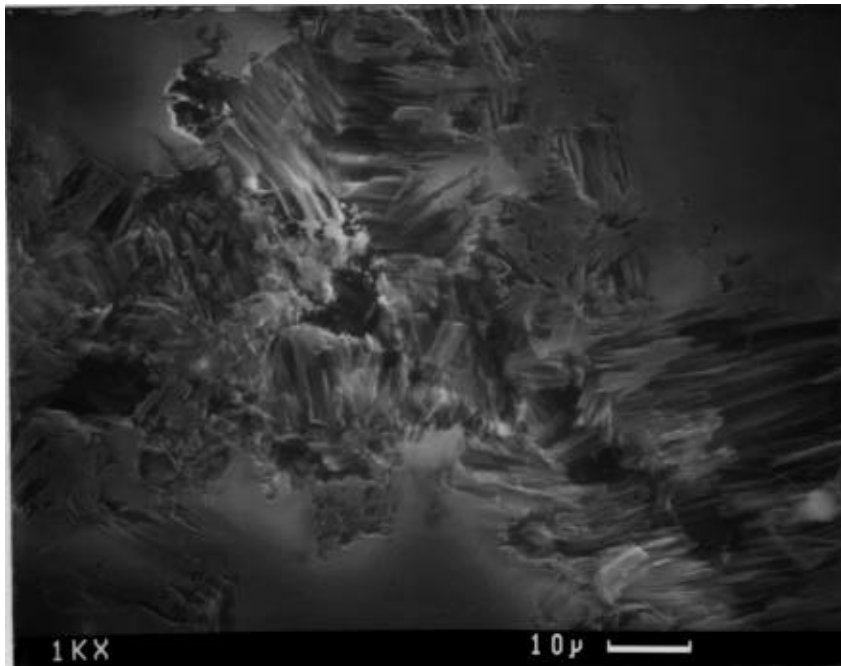


Figure 5. Scanning electron micrograph of pitted beryllium showing distinct planes in corrosion pits. These planes appear to be the (0001) basal planes.

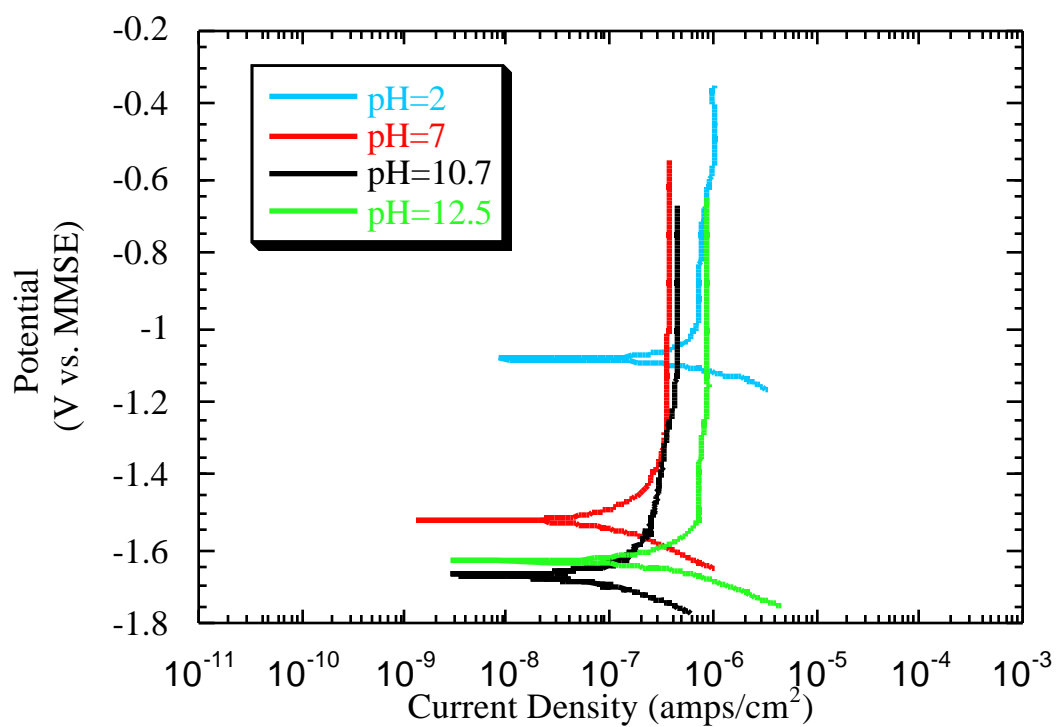


Figure 6. Beryllium polarization curves as a function of solution pH. Beryllium forms a passive layer and does not pit in the absence of an aggressive species.

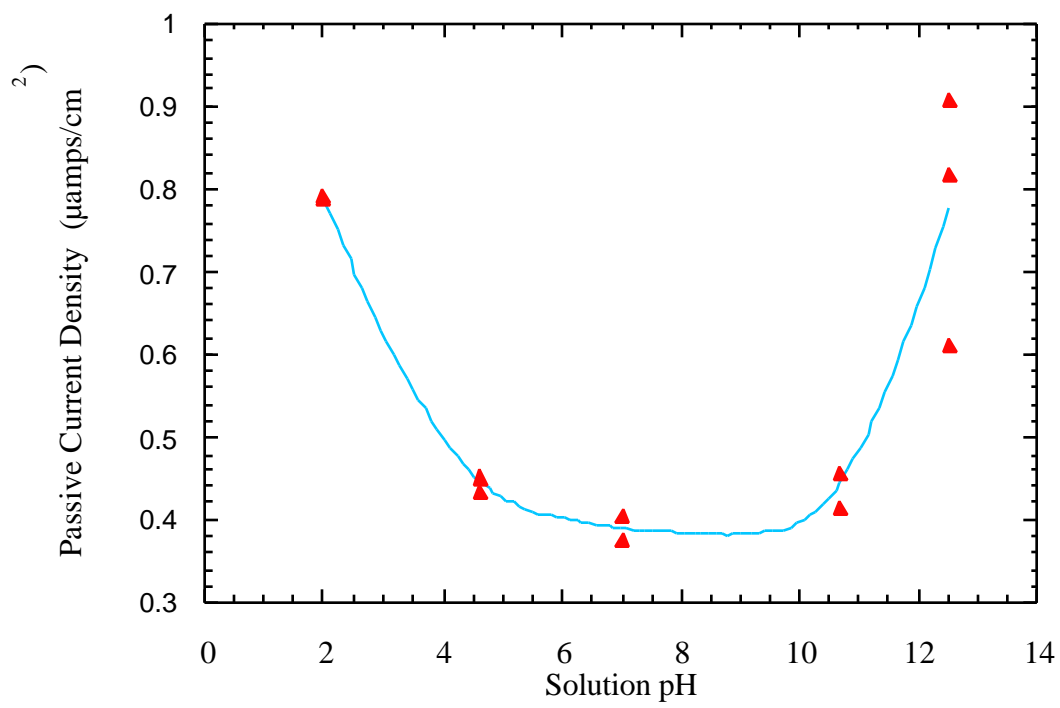


Figure 7. Passive current density as a function of pH showing a minimum in the pH range between 7 and 9.

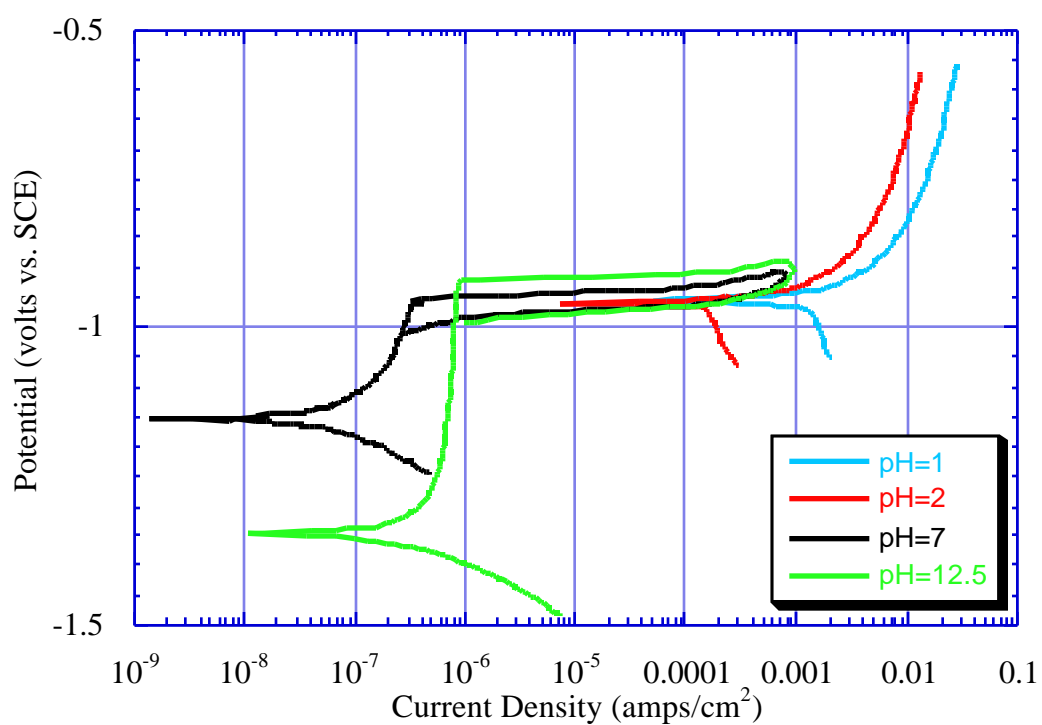


Figure 8. Potentiodynamic polarization curves as a function of chloride concentration and pH. The beryllium pits at pHs of 7 and 12.5 and actively dissolves at pHs of 1 and 2.

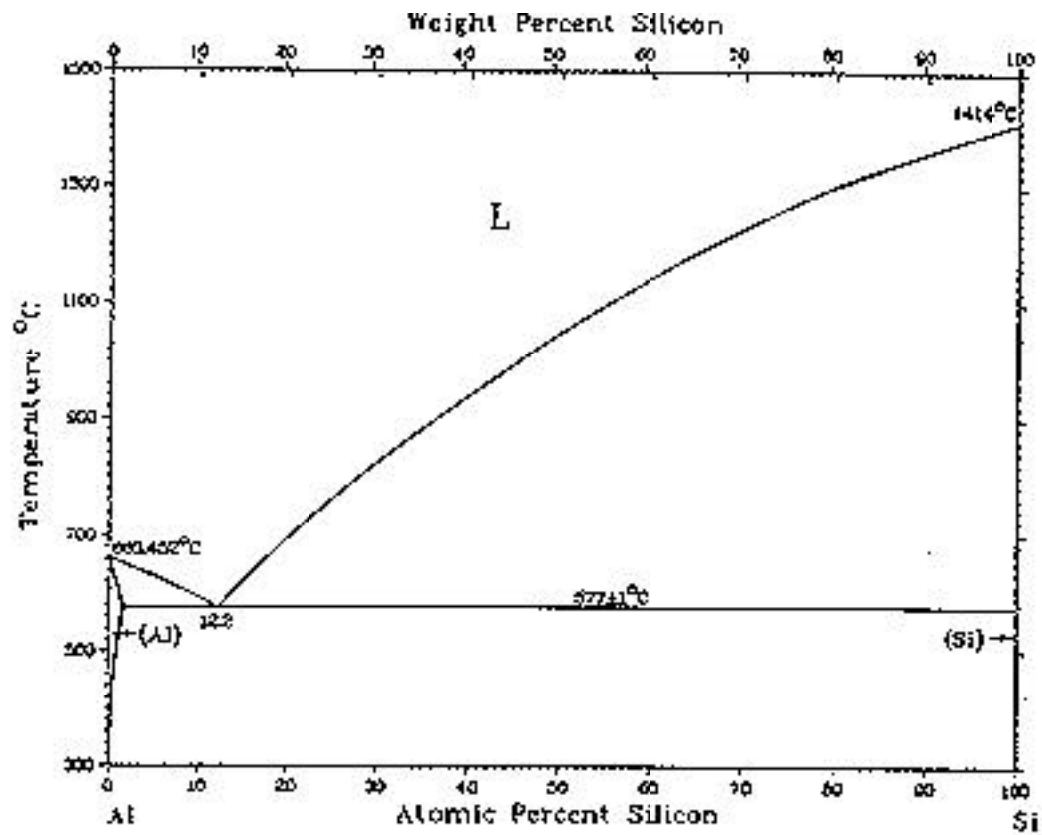


Figure 9. Aluminum-Silicon Phase Diagram showing the eutectic at 12.2 at.% Si. (28)

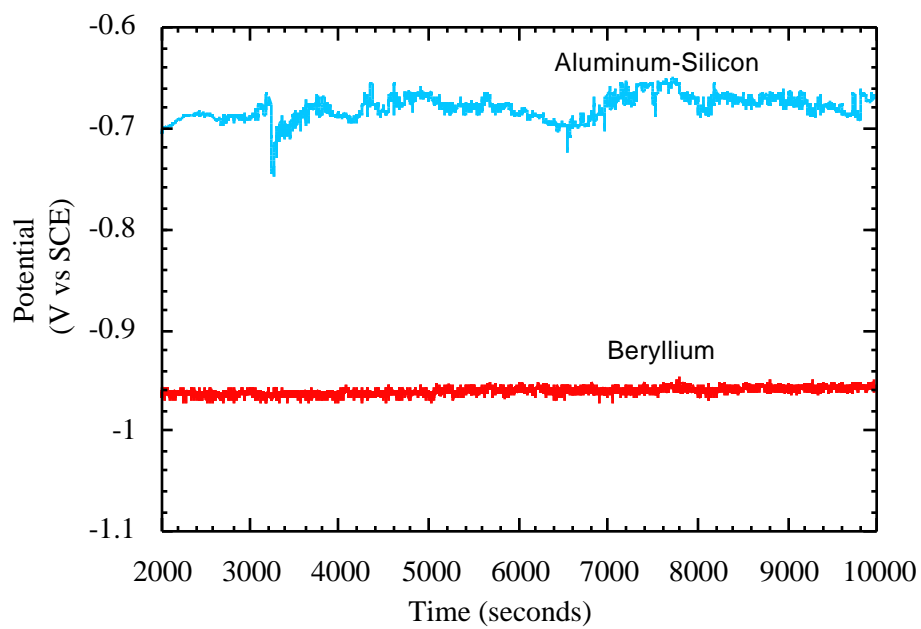


Figure 10. Open circuit potential of Be and Al-Si as a function of time in 0.1 M NaCl under ambient aeration.

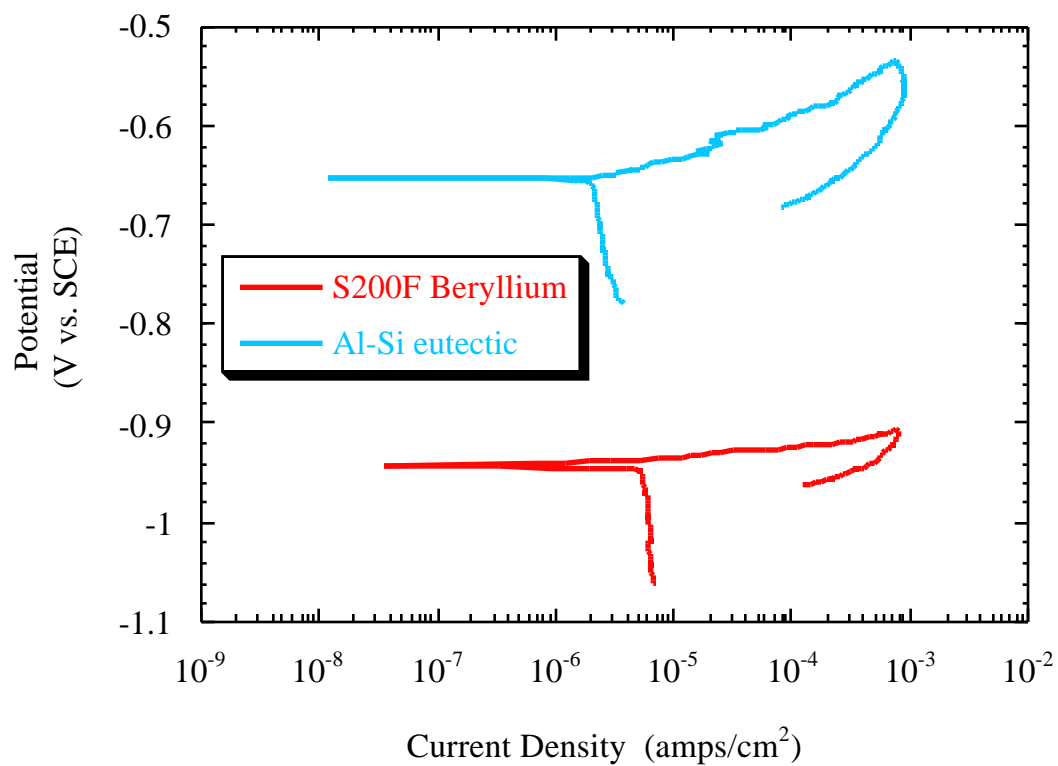


Figure 11. Polarization curves of Al-Si and beryllium in 0.1 M NaCl under ambient aeration. If the cathodic line of the aluminum-silicon were extended, it would eventually intersect the anodic curve of the beryllium at the couple current and couple potential.

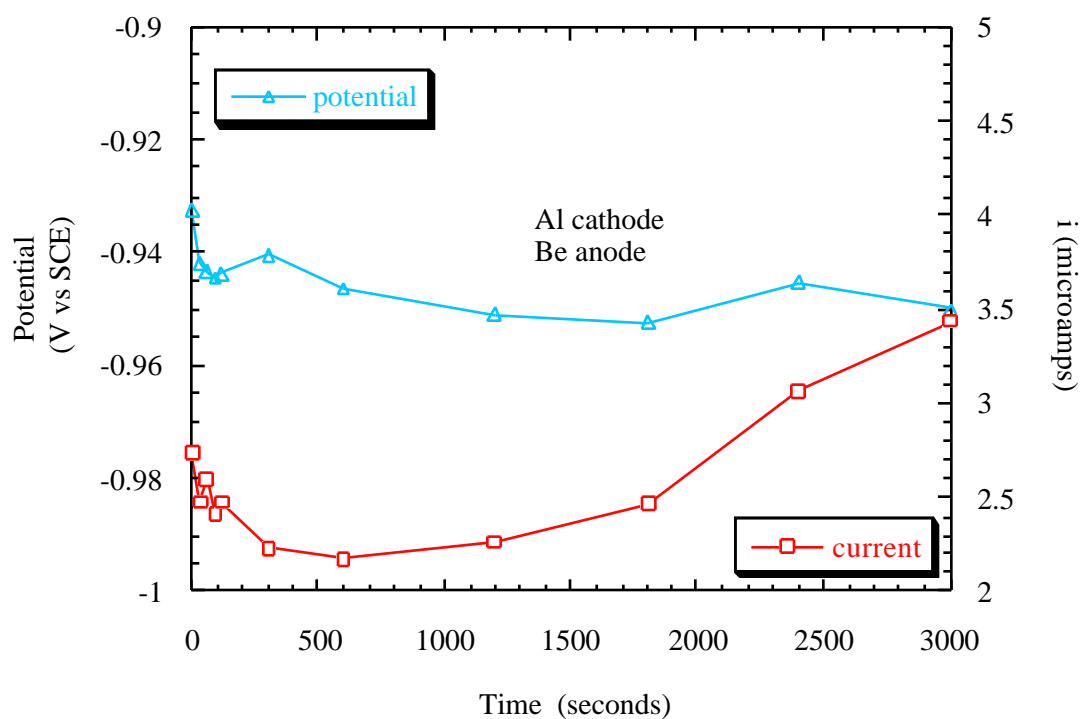


Figure 12. Couple potential and couple current as a function of time for an aluminum/silicon-beryllium galvanic couple in 0.1 M NaCl under ambient aeration.

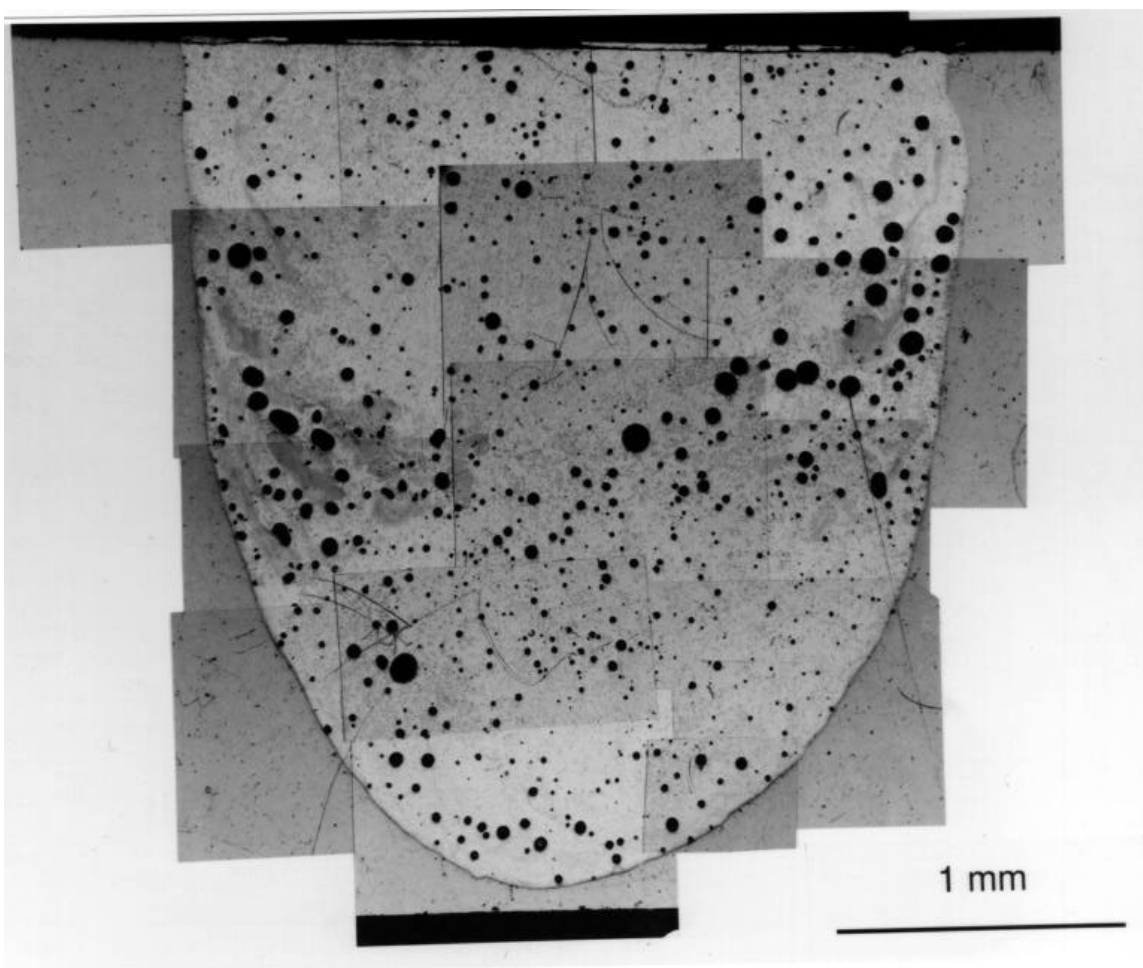


Figure 13a. Bright field optical micrograph of beryllium weldment prior to immersion in chloride solution.

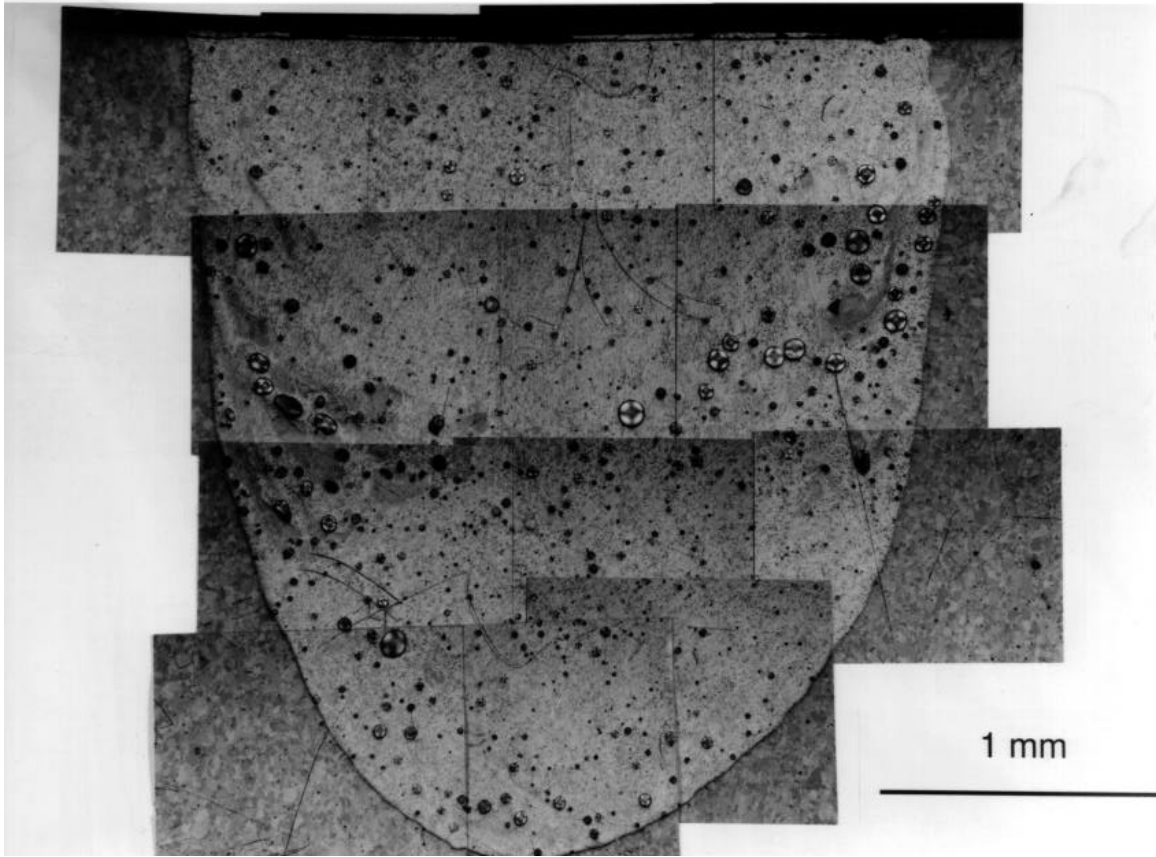


Figure 13b. Polarized light optical micrograph of beryllium weldment prior to immersion in chloride solution.

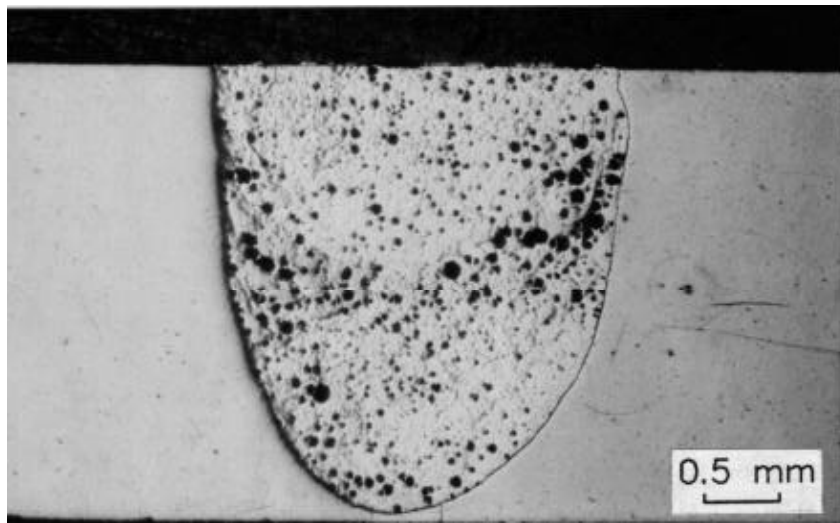


Figure 14. Bright field optical micrograph of beryllium weldment following two hours of immersion in 0.1 M NaCl solution.

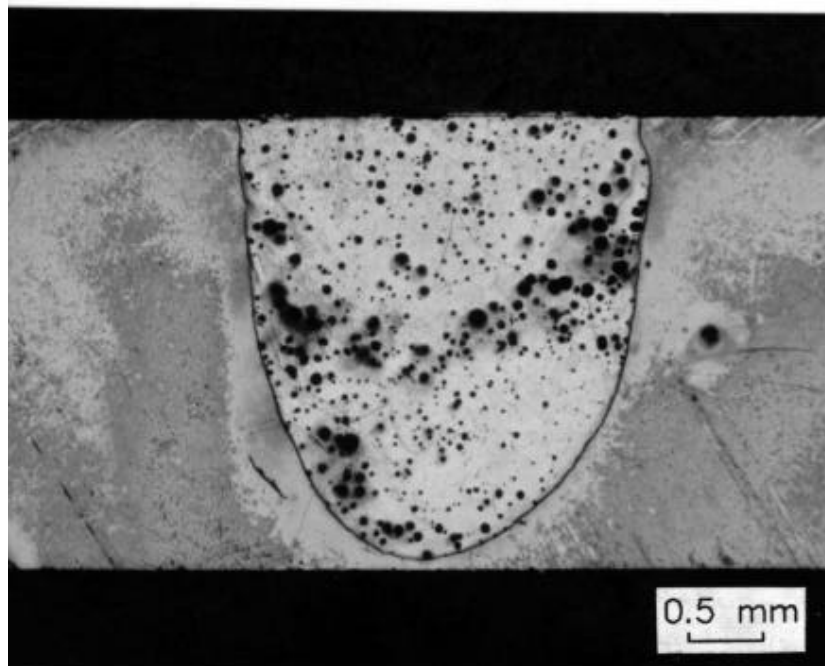


Figure 15. Bright field optical micrograph of beryllium weldment following two days of immersion in 0.1 M NaCl solution .

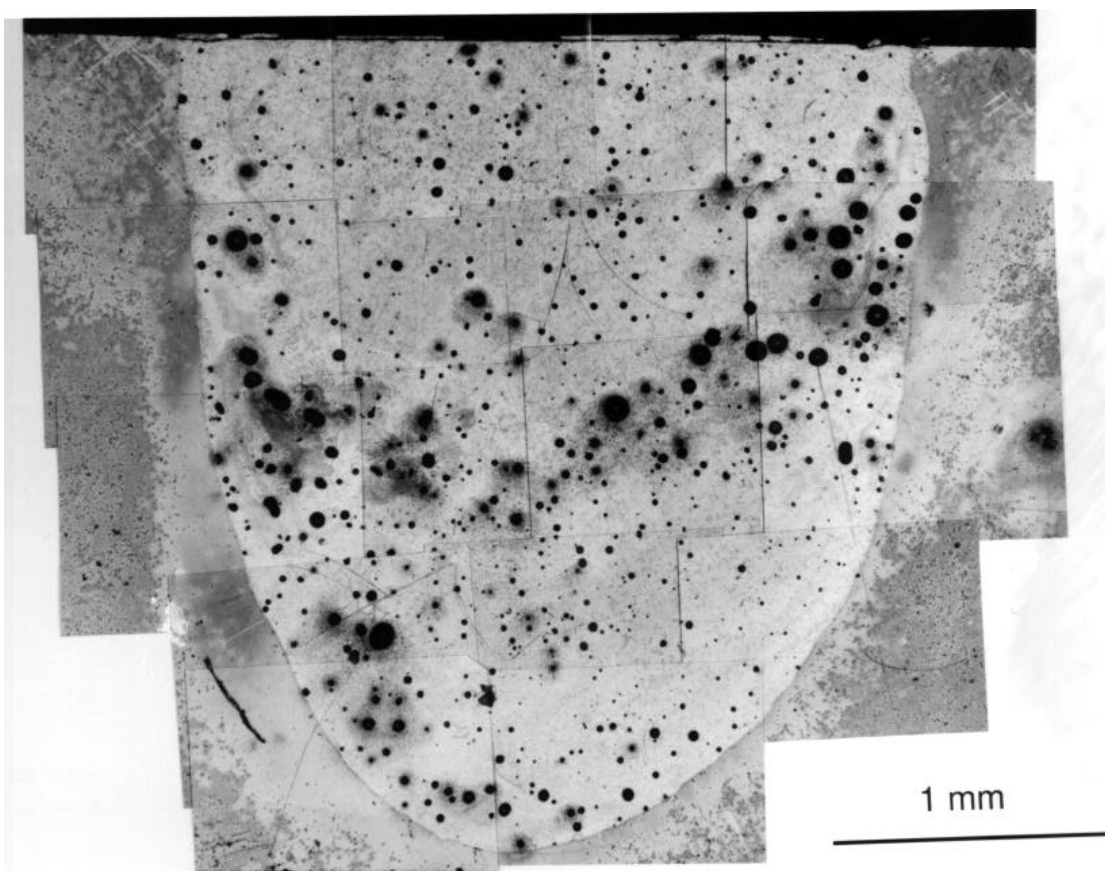


Figure 16. Bright field optical micrograph of beryllium weldment following two days of immersion in 0.1 M NaCl solution.

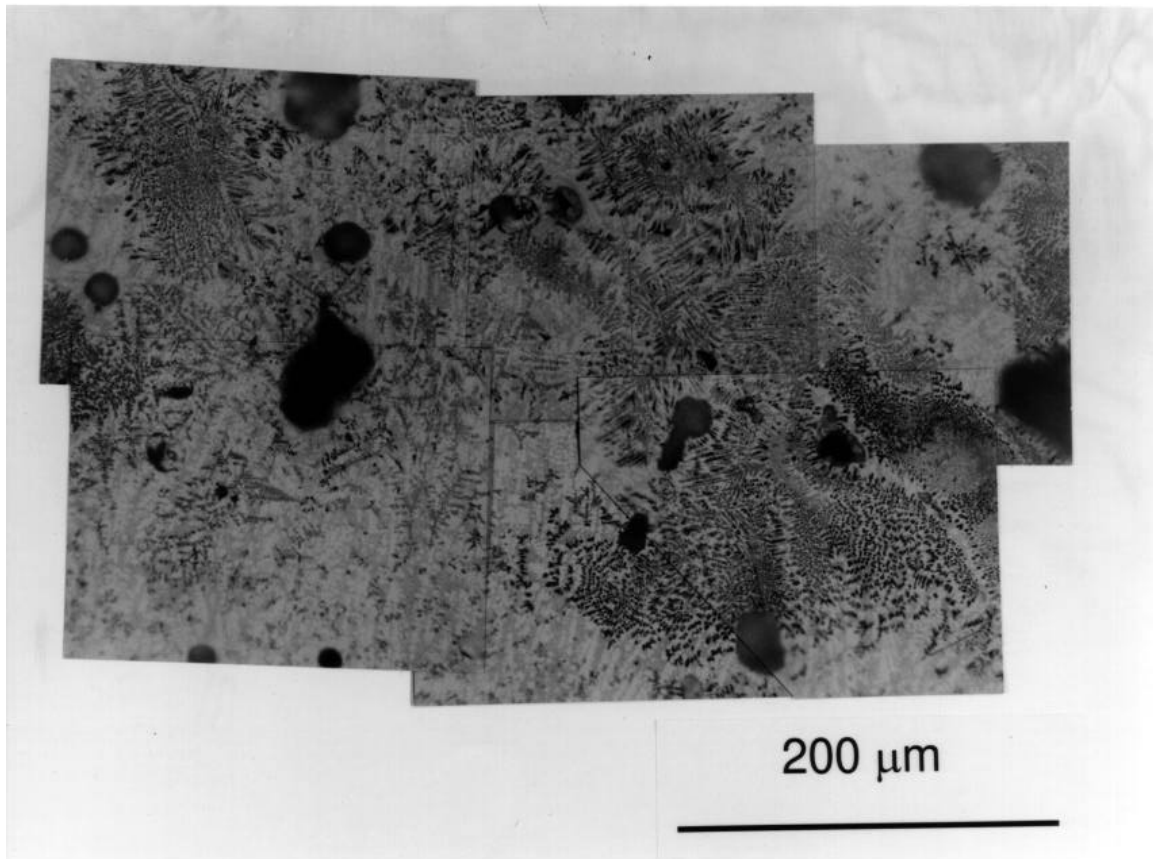


Figure 17. Preferential attack of beryllium precipitates in Al-Si weld bead.

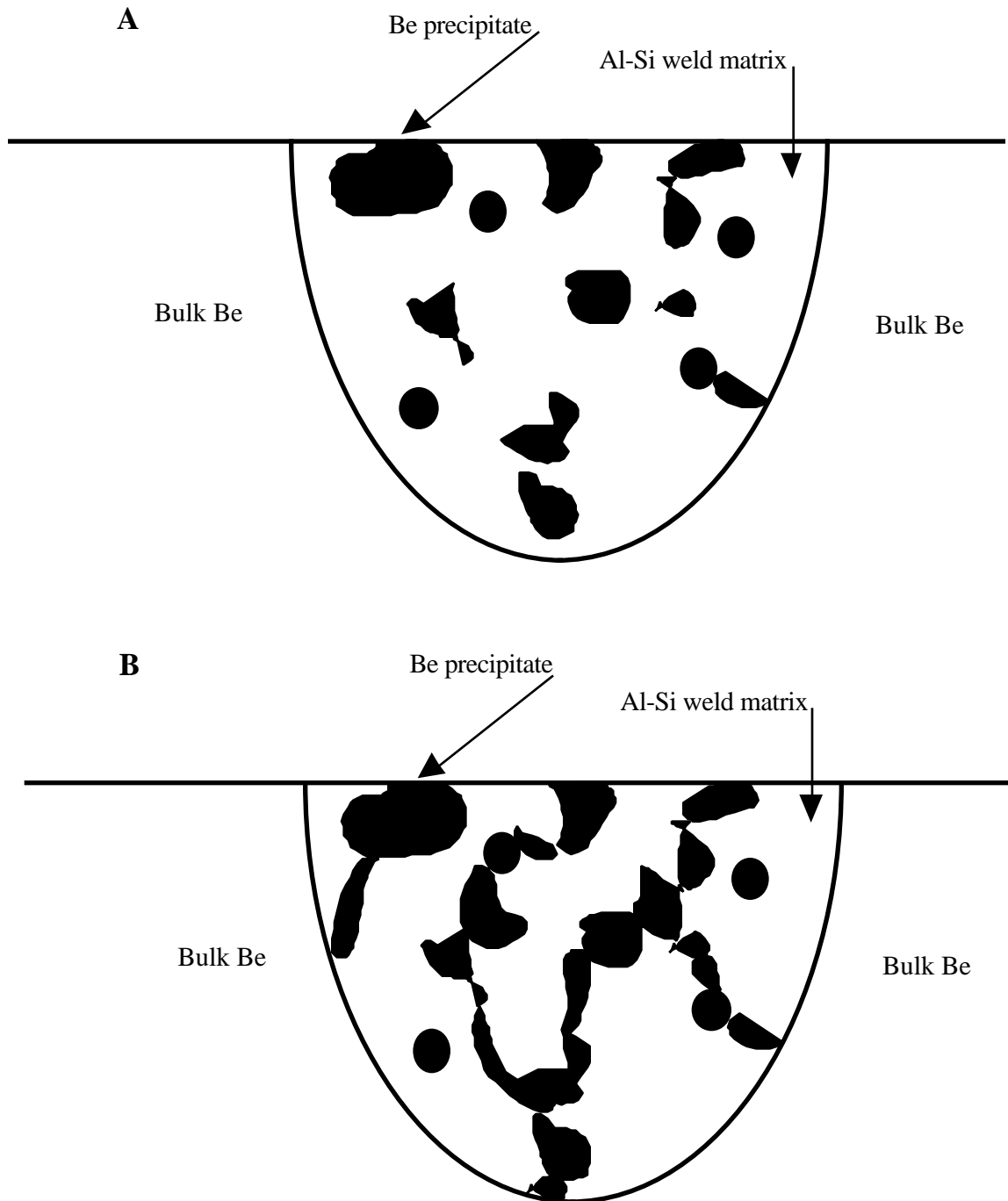


Figure 18. Diagram representing concentrations of Be precipitates in the weld matrix which are **a)** below the percolation threshold for weld deterioration and **b)** above the percolation threshold for weld deterioration.

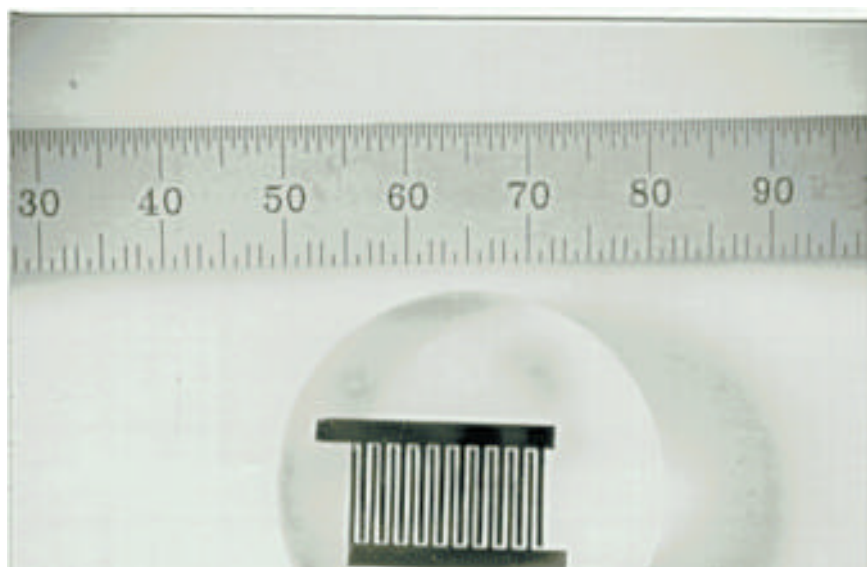


Figure 19. Photograph displaying an atmospheric corrosion monitor made of laser machined mild steel and titanium.

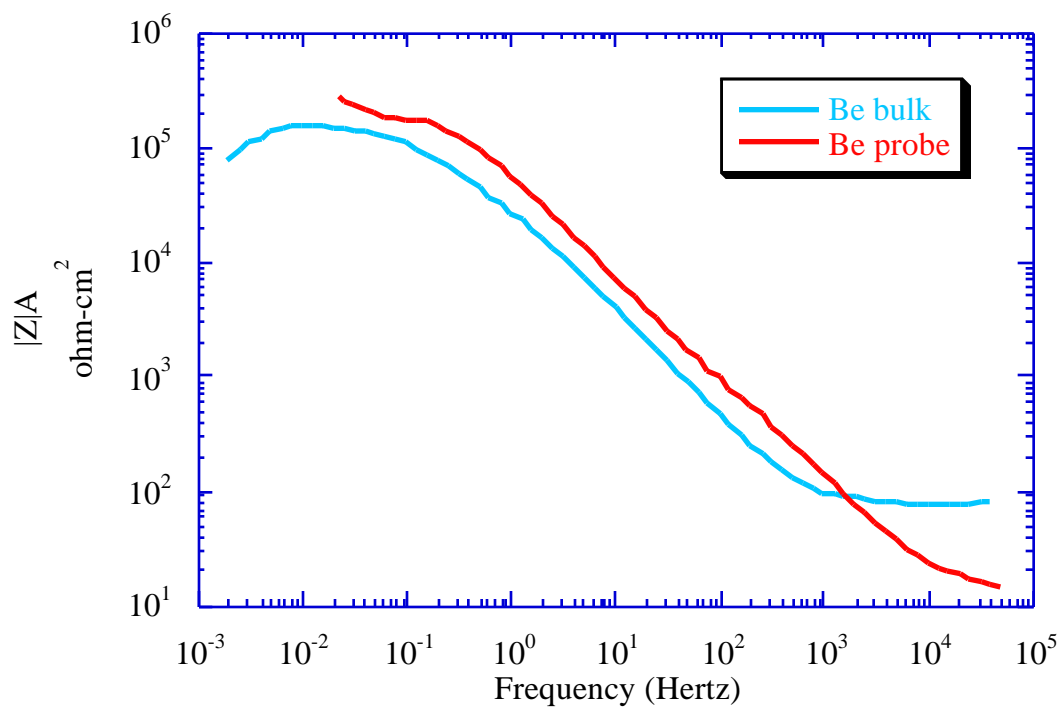


Figure 20. Electrochemical impedance microscopy measurements on a beryllium corrosion monitor as compared with a bulk beryllium sample. The bulk sample was submersed in a boric acid/borate (pH=7) solution while a drop of solution approximately 1.6 cm in diameter was placed on the monitor. Results did not differ significantly between the bulk sample and the monitor.

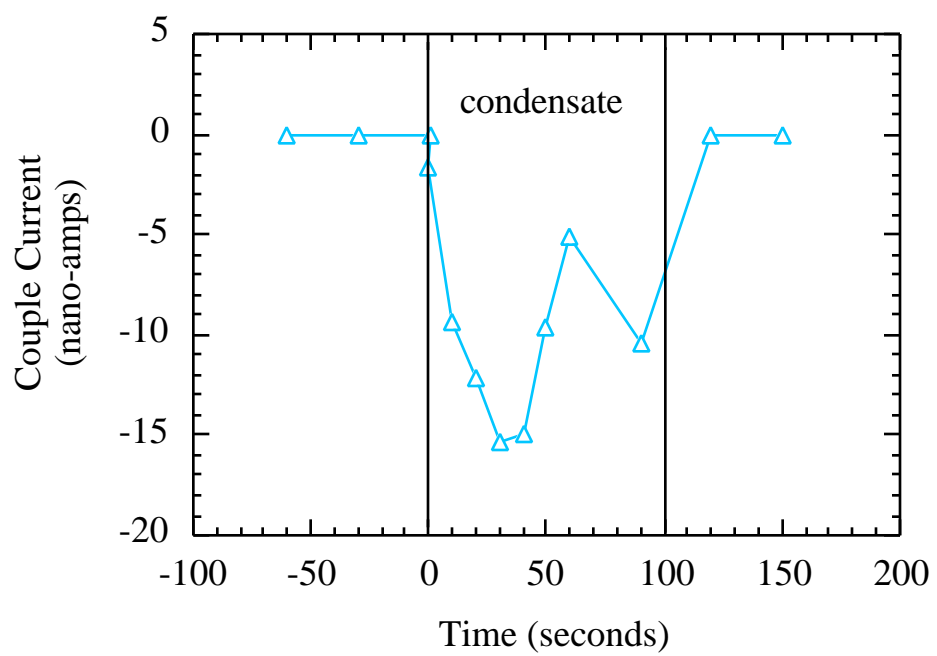


Figure 21. Couple current measured on a titanium/mild steel corrosion monitor with thin beads of water on the surface.